JACS
JOURNAL OF THE AMERICAN CHEMICAL SOCIETY
pubs.acs.org/JACS
Article

# Surface-Promoted Evolution of Ru-bda Coordination Oligomers Boosts the Efficiency of Water Oxidation Molecular Anodes

Marcos Gil-Sepulcre, Joachim O. Lindner, Dorothee Schindler, Lucía Velasco, Dooshaye Moonshiram, Olaf Rüdiger, Serena DeBeer, Vladimir Stepanenko, Eduardo Solano, Frank Würthner,* and Antoni Llobet*

Cite This: J. Am. Chem. Soc. 2021, 143, 11651−11661
Read Online
ACCESS | Metrics & More | Article Recommendations | Supporting Information

**ABSTRACT:** A new Ru oligomer of formula {[$Ru^{II}$(bda-κ-$N^2O^2$)-(4,4′-bpy)]$_{10}$(4,4′-bpy)}, **10** (bda is [2,2′-bipyridine]-6,6′-dicarboxylate and 4,4′-bpy is 4,4′-bipyridine), was synthesized and thoroughly characterized with spectroscopic, X-ray, and electrochemical techniques. This oligomer exhibits strong affinity for graphitic materials through CH−π interactions and thus easily anchors on multiwalled carbon nanotubes (CNT), generating the molecular hybrid material **10@CNT**. The latter acts as a water oxidation catalyst and converts to a new species, **10′$(H_2O)_2$@CNT**, during the electrochemical oxygen evolution process involving solvation and ligand reorganization facilitated by the interactions of molecular Ru catalyst and the surface. This heterogeneous system has been shown to be a powerful and robust molecular hybrid anode for electrocatalytic water oxidation into molecular oxygen, achieving current densities in the range of 200 mA/cm$^2$ at pH 7 under an applied potential of 1.45 V vs NHE. The remarkable long-term stability of this hybrid material during turnover is rationalized based on the supramolecular interaction of the catalyst with the graphitic surface.

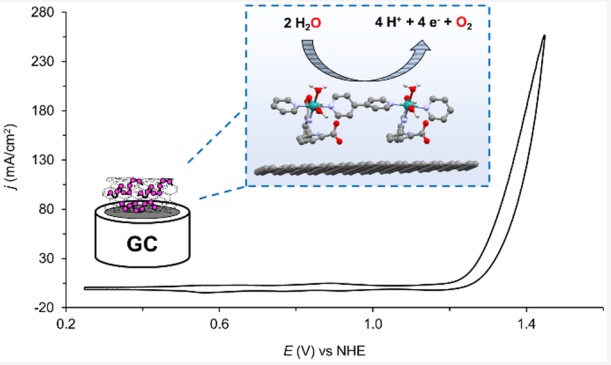


## INTRODUCTION

The design of an efficient artificial photosynthetic device for water splitting has been one of the hot topics during the past decade for the scientific community because such devices can provide access to clean and renewable energy sources as an alternative to fossil fuels. This in turn could contribute to solving the problems of global warming and climate change faced by our modern society today.[1−4] Water splitting with sunlight can be achieved using photoelectrochemical cells that accomplish water oxidation at the anode and proton reduction at the cathode. From the anode perspective, a key issue is the use of robust and efficient water oxidation catalysts (WOCs) anchored on a conductive or semiconductive surface. This is a challenging issue because of the considerably unfavorable thermodynamics and complex mechanism, which generally result in large activation energies associated with the water oxidation reaction.[5]

Two main strategies have been employed up to now toward the development of efficient electro(photo) anodes based on the use of metal oxides (MOx) or molecular complexes as WOCs deposited on the surface of a (photo)electrode.[6−8] Efficient electro(photo) anodes based on metal oxides as WOCs is mainly limited to pH 13 or above, and in general a large amount of MOx is needed.[9,10] On the other hand, molecular catalysts can be used at a broader pH range[11−17] and their stability is highly dependent on the anchoring strategy. However, their performance is normally limited by the amount of active catalyst that can be deposited per surface area.[18−20]

The best molecular WOCs reported today are based on Ru complexes containing equatorially coordinating pyridyl-carboxylate ligands and monodentate pyridyl groups completing the axial positions. In particular, [Ru(bda)(isoq)$_2$] (bda is [2,2′-bipyridine]-6,6′-dicarboxylate; isoq is 8-isoquinoline) and [Ru(tda)(py)$_2$] (tda is [2,2′:6′,2″-terpyridine]-6,6″-dicarboxylate; py is pyridine), abbreviated from now on as Ru-bda and Ru-tda, achieve turnover frequency (TOF) values in the range of 1000−50 000 s$^{-1}$, respectively, in the homogeneous phase.[21−25] Interestingly, homologues of these molecular catalysts have been successfully anchored on surfaces, although their performances as WOCs are markedly different.[26−28] While Ru-tda shows a robust performance with current densities in the range of 5 mA/cm$^2$,[28] Ru-bda decomposes to form RuOx mainly due to the absence of a bimolecular O−

Received: May 7, 2021
Published: July 22, 2021

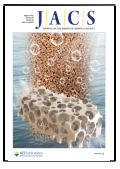







https://doi.org/10.1021/jacs.1c04738
J. Am. Chem. Soc. 2021, 143, 11651−11661

O bond formation pathway (I2M mechanism; interaction of two M−O units) under restricted mobility conditions, that is, its low-energy pathway.[29]

Recently, a family of Ru-tda-based oligomers of general formula $\{[Ru^{II}(tda\text{-}\kappa\text{-}N^3O)(4,4'\text{-bpy})]_n(4,4'\text{-bpy})\}$ (4,4′-bpy is 4,4′-bipyridine; $n$ = 1, 2, 4, 5, and 15), abbreviated as $(Ru\text{-}tda)_{15}$, has been prepared, isolated, and thoroughly characterized in homogeneous solution. These oligomers display an outstanding affinity for graphitic surfaces such as multiwalled carbon nanotubes (CNTs), thanks to multiple ligand-based CH−$\pi$ interactions with the graphitic surfaces.[30] The new molecular hybrid materials display an impressive water oxidation electrocatalytic activity with unprecedented current densities, for anchored molecular catalysts, in the range of 200−300 mA/cm$^2$ at 1.45 V vs NHE at pH 7.

The outstanding performance displayed by the Ru-tda oligomers anchored on graphitic surfaces inspired us to explore the performance of a new decameric Ru-bda oligomer, $\{[Ru^{II}(bda\text{-}\kappa\text{-}N^2O^2)(4,4'\text{-bpy})]_{10}(4,4'\text{-bpy})\}$, **10**, as an electrocatalyst for water oxidation as well as to explore its mechanism of action under restricted mobility conditions. It is important to keep in mind here that the monomeric Ru-bda complexes anchored to solid supports undergo decomposition to $RuO_2$ under restricted mobility conditions as mentioned above.[29] Toward this goal, we were encouraged by our recent successful research on anodes[31] prepared from macrocyclic trimer $\{[Ru(bda)]_3(\mu\text{-bpb})_3\}$, **MC3** (bpb is 1,4-bi(pyridin-3-yl)-benzene), that changed the O−O bond formation mechanism from I2M to water nucleophilic attack (WNA) by a supramolecular effect and thereby circumvented the handicaps associated with the restricted mobility.[32] We reasoned that the combination of these two phenomena, i.e., on one hand the enhanced performance of the oligomers and on the other hand the change of the O−O bond formation mechanism by environmental perturbations, should lead to new interesting molecular hybrid materials.

Indeed, our detailed experimental and theoretical studies revealed that the newly synthesized Ru-bda linear oligomer $\{[Ru^{II}(bda\text{-}\kappa\text{-}N^2O^2)(4,4'\text{-bpy})]_{10}(4,4'\text{-bpy})\}$, **10**, can be successfully anchored on CNTs via noncovalent CH−$\pi$ interactions, and the respective molecular hybrid anode exhibited excellent catalytic performance in water oxidation, possessing outstanding stability.

## RESULTS AND DISCUSSION

**Synthesis, Characterization, and Graphitic Affinity of 10.** The Ru-bda-based oligomer **10** (for structure see Figures 1, top, and 3) was synthesized by refluxing an equimolar solution of $[Ru(bda)(DMSO)_2]$ and 4,4′-bpy in TFE−MeOH, 9:1 (TFE is 2,2,2-trifluoroethanol), at 78 °C for 3 days (details are provided in the Supporting Information (SI)). The new oligomer was characterized by 1D and 2D NMR spectroscopy (Figures 1 and S5), UV−vis (Figure S12), mass spectrometry (Figures S10 and S11), elemental analysis, resonance Raman spectroscopy (Figures S33 and S34), powder X-ray diffraction (Figure S13), and electrochemical techniques in organic solvents (Figures S14 and S15). $^1$H NMR is particularly useful because it allows differentiating between resonances of the bridging and terminal 4,4′-bpy ligands and thus enables the calculation of the number of repetitive units that turned out to be 10 and thus is labeled as **10** (Figure 1). Thus, oligomer **10** has a length of approximately 12.0 nm and a width of 0.9 nm based on the typical bonding distances for Ru-bda complexes

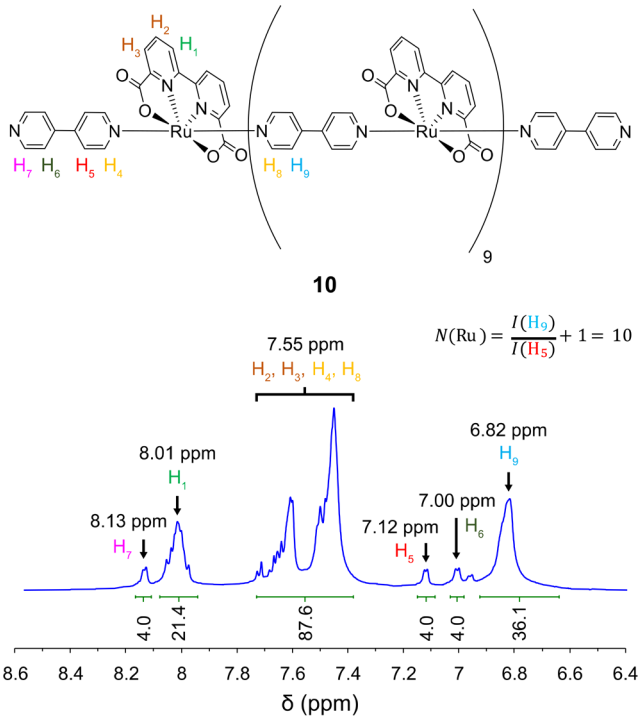


**Figure 1.** Chemical structure and $^1$H NMR spectrum (500 MHz, 298 K, [$d_3$]-TFE) of $\{[Ru(bda)(4,4'\text{-bpy})]_{10}(4,4'\text{-bpy})\}$ (**10**) oligomer. The number of Ru units in the oligomer, $N$(Ru), was determined from the integrals over $H_9$ and $H_5$ signals, $I(H_9)$ and $I(H_5)$.

(see the SI). Furthermore, a DOSY experiment shows the presence of only one species in solution and thus indicates that there is no oligodispersity (see Figure S6). An optimized structure of oligomer **10** in the gas phase was calculated using the PM6-D3H4 method to visualize its molecular structure and dimensions (see Figure 3).

Oligomer **10**, as also the case for related homologues containing the Ru-tda unit,[30] has a strong affinity for graphitic surfaces due to its multiple interaction sites. Indeed, upon addition of a reddish solution of **10** in TFE to a tetrahydrofuran (THF) suspension containing CNTs at room temperature (RT), the solution immediately decolorizes, clearly indicating adsorption of **10** onto the CNTs, forming the molecular hybrid material **10@CNT** (Figure S4). Similarly, when a THF solution of **10** is in contact with a glassy carbon electrode disk ($GC_d$; $S$ = 0.07 cm$^2$), it also strongly adsorbs at the electrode, forming the material **10@GC**. The presence of **10** anchored on the graphitic surfaces can be readily observed using electrochemical techniques, as can be seen in Figures S1 and S2. The electrochemical performance of **10** anchored on graphitic supports was analyzed based on cyclic voltammetry (CV), differential pulse voltammetry (DPV), and controlled potential electrolysis (CPE) techniques. All electrochemical experiments were carried out in 1 M phosphate buffer at pH 7 and reported vs NHE. The CVs of **10@GC** or **10@CNT@GC** (where **10@CNT** is drop-casted at the $GC_d$ electrode; see the SI for details) display the typical redox waves associated with the III/II, IV/III, and V/IV couples that have been previously described for the $[Ru(bda)(pic)_2]$, **1-pic**,[22] monomer in homogeneous phase, although with smaller peak splitting due to its restricted mobility (see SI, Figures S17, S20A, and S24 and Tables S1 and S2). This confirms that the nature of the oligomeric species anchored on the graphitic surface is the


https://doi.org/10.1021/jacs.1c04738
J. Am. Chem. Soc. 2021, 143, 11651−11661

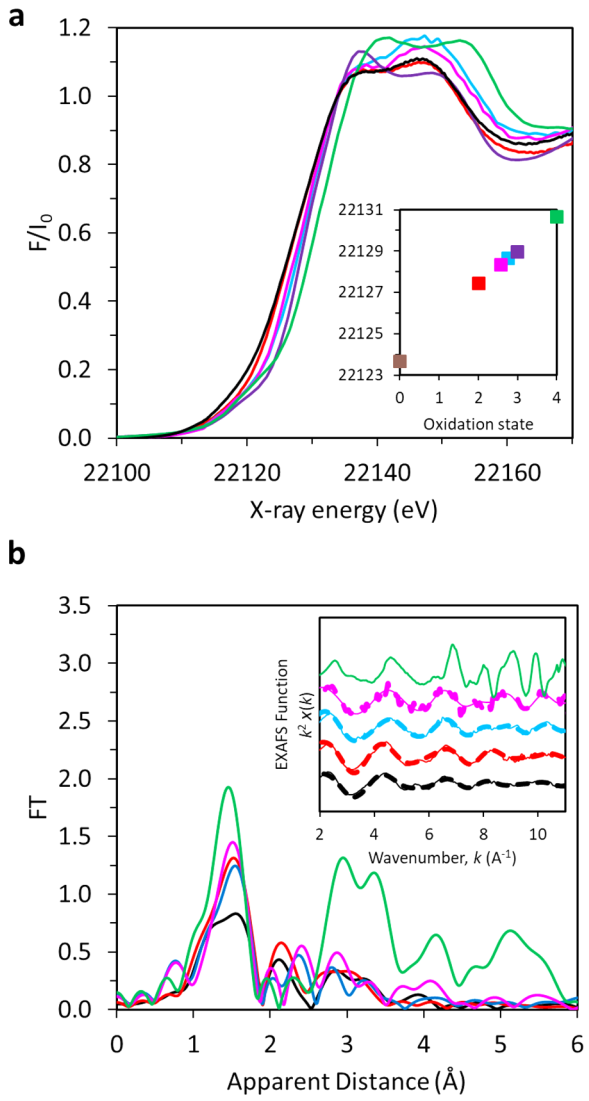


**Figure 2.** (a) Normalized Ru K-edge XANES for **10** (black line), **10@CNT@GC$_p$** (red line), **10′(H$_2$O)$_2$@CNT@GC$_p$** (cyan line), **10′(H$_2$O)$_2$@CNT@GC$_p$** after catalysis (magenta line), [Ru(tda)-(Py)$_2$] (purple line), and $RuO_2$ (green line). (b) Fourier transforms of $k^2$-weighted Ru EXAFS for **10** (black line), **10@CNT@GC$_p$** (red line), **10′(H$_2$O)$_2$@CNT@GC$_p$** (cyan line), and **10′(H$_2$O)$_2$@CNT@GC$_p$** after catalysis (magenta line) and $RuO_2$ (green line). Inset: Back Fourier transformed experimental (solid lines) and fitted (dashed lines) $k_2[\chi(k)]$ of Ru complexes together with $RuO_2$ (green). Experimental spectra were calculated for $k$ values of 2−11 Å$^{-1}$.

same as in the homogeneous phase. The electrochemical experiments are also instrumental since they allow calculating quantitatively the amount of sample deposited at the surface of the electrode as well as its surface coverage. For **10@GC**, a surface coverage of 73% is obtained (see Figure S2 in the SI), suggesting the formation of less than a monolayer and thus excluding agglomeration of oligomers at the surface.

Furthermore, X-ray absorption near edge structure (XANES) and extended X-ray absorption fine structure (EXAFS) techniques were applied in order to spectroscopically characterize the new hybrid materials. Figure 2 shows XANES spectra of **10** as a powder and anchored on CNTs, which in turn have been deposited on the surface of a glassy carbon plate (GC$_p$) by drop-casting to give **10@CNT@GC$_p$**. The half-edge energies obtained revealed that the Ru center remains at oxidation state II before and after anchoring onto the CNTs. The simulated and experimental EXAFS spectra for both samples show the expected octahedral coordination environment surrounding the Ru center with two Ru−N$_{bda}$ at 1.90−1.91 Å and four Ru−N/O at 2.07−2.08 Å, which are slightly elongated to Ru−N/O at 2.07 Å after anchoring to the CNTs (Tables S5−S7). These distances are also in proper agreement with the X-ray structure of the monomeric [Ru(bda)(pic)$_2$][21] and with the calculated structures of monomeric model compound [Ru(bda)(py)$_2$] (Figure S42) and oligomer **10** (Figure 3).

This new material was also characterized by microscopy techniques including atomic force microscopy (AFM), scanning electron microscopy (SEM), and energy dispersive X-ray spectroscopy (EDX). The AFM experiments in Figure 4

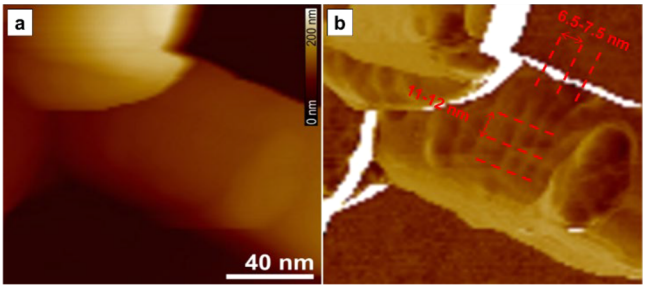


**Figure 4.** Height (a) and phase (b) AFM images of **10@CNT**. Z scale is 200 nm. The images show a fragment of a carbon nanotube covered by thin rod-like particles of about 11−12 nm length.

show images of **10@CNT** with the fragments of CNTs covered by thin rod-like particles with a length of ca. 11−12 nm, which is within the 11.96 nm expected distance of **10** (see Figure 3 and Figure S2 in the SI). The oligomers are oriented parallel to one another on the CNT surface, and the distance between two neighboring particles measured middle-to-middle varies between 6.5 and 7.5 nm. Considering the tip-broadening effect for AFM with a nominal tip radius of 7 nm used for these experiments, we can assume that each rod-like nanoparticle corresponds to an oligomer of **10**. Further combined SEM/EDX investigations of the thin **10@CNT** film spin-coated onto a silicon wafer are also consistent with the presence of the oligomer anchored on the CNT (Figure S41).

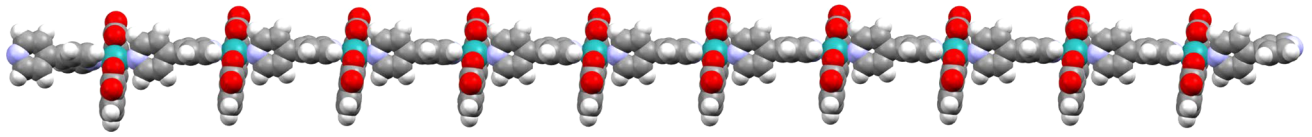

**Figure 3.** Space-filling structure of oligomer **10** in the gas phase calculated based on the PM6-D3H4 method. Color code: Ru, light blue; O, red; N, blue; C, gray; H, white. In this model the distance between the N atoms in the extremes of the oligomer (nonbonded to Ru) turns out to be 11.96 nm.



https://doi.org/10.1021/jacs.1c04738
J. Am. Chem. Soc. 2021, 143, 11651−11661

As proposed earlier for a related homologue,[30] a nearly perpendicular CH−$\pi$ interactions between the 60 CH groups (H1, H2, and H3 in Figure 1, top, and their symmetric counterparts) of the 10 bda ligands in **10** with the delocalized $\pi$-system of the graphitic material are responsible for the strong affinity of **10** toward graphitic surfaces such as graphite and CNTs (see Figure S46 for a drawing of this interaction). The existence of this CH−$\pi$ interaction was monitored in solution by $^1$H NMR spectroscopy using **1-pic** and 1-pyrenebutanol (pyn-OH) as low molecular weight models of **10** and the graphitic surface, respectively. Figures S7−S9 show that when a $d_4$-MeOD solution of **1-pic** and pyn-OH are mixed, their aromatic resonances shift within the range of 0.01 ppm due to the mentioned interactions, whereas the aliphatic ones remain virtually unaltered.

Grazing incident wide-angle X-ray scattering (GIWAXS) experiments were employed to characterize the interaction of **10** with graphitic surfaces. As can be observed in Figure 5 and

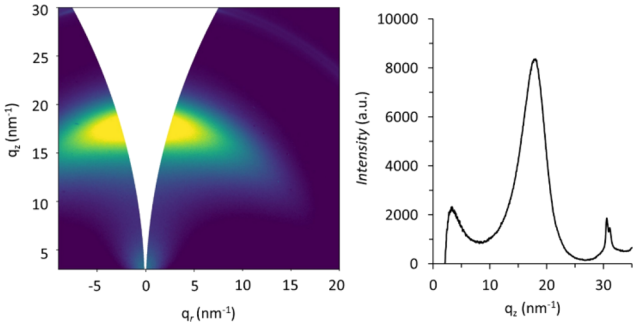


**Figure 5.** (Left) 2D GIWAXS blank-subtracted scattering pattern of **10@GC$_p$** and (right) the corresponding $q_z$ 1D cut profile near the specular direction.

Figure S38, 2D GIWAXS patterns obtained for **10** anchored on a flat glassy carbon plate electrode display an anisotropic broad band associated with a preferential face on orientation of **10** on GC$_p$, also consistent with the results obtained from AFM and NMR and further supported by DFT calculations. The 1D cut displayed on the right-hand side reveals an oligomer−surface distance in the range of 2.8−6.2 Å (10−22 nm$^{-1}$ in reciprocal space).[30] These observations, together with the parallel orientation of the monomers revealed by AFM, and a coverage below a monolayer strongly support that CH−$\pi$ interactions are responsible for the high affinity of **10** for graphitic surfaces.

To further corroborate these experimental evidence and complement them, we carried out density functional theory (DFT) as well as semiempirical calculations. In this work all DFT calculations were performed using the B3LYP functional,[33−35] together with a proper implicit solvation model and, where needed, explicit water molecules, as described in detail in the SI. Figure 6 (top) shows an image of the calculated interactions of a dimeric Ru model {[Ru$^{II}$(bda-$\kappa$-N$^2$O$^2$)(py)]$_2$($\mu$-4,4′-bpy)}, **2**, anchored on a hexagonal graphene sheet surface, **2@GS**, where the CH−$\pi$ interactions can be visualized. The resulting interaction between the surface and the dimer is exergonic by 32.6 kJ/mol.

**Surface-Promoted Transformation of 10@CNT to 10′(H$_2$O)$_2$@CNT.** The performance of **10@CNT** was initially analyzed based on 50 repetitive CV scans in the potential range of 0.25−1.45 V at pH 7 (Figure 7a and Figure S16). After each scan the intensity of the catalytic wave at $E_{onset}$ = 1.02 V

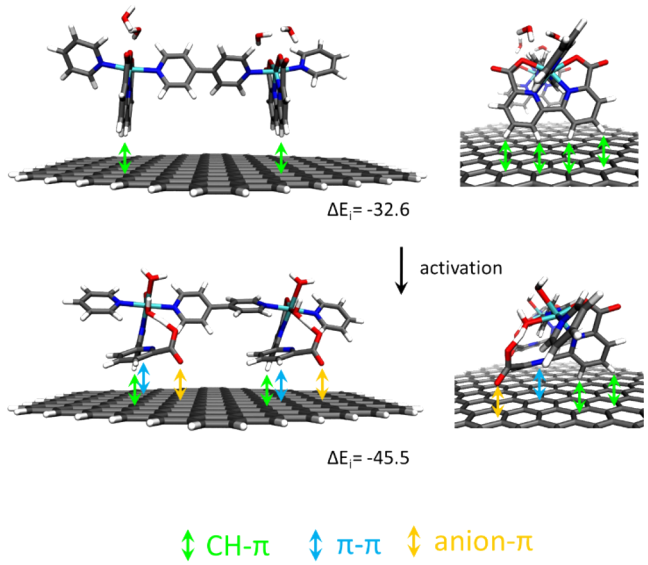


**Figure 6.** Schematic representation of noncovalent interactions in a dimer model of **10@CNT@GC** before (top) and after activation (bottom) with semiempirically calculated interaction energies per Ru center ($\Delta E_i$) in kJ/mol.

(assigned to the V/IV) decreases, while the onset of the foot of the catalytic wave progressively increases, which is a clear indication that the initial active species is transformed into a new catalytic species (Figure S17). Furthermore, the non-catalytic waves that appear at potentials $E_{1/2}$ = 0.73 V (III/II, $\Delta E$ = 28 mV) and $E_{1/2}$ = 0.89 V (IV/III $\Delta E$ = 23 mV) similar to the monomer disappear and a new set of redox couples appears in the voltammogram at $E_{1/2}$ = 0.62 V (III/II, $\Delta E$ = 34 mV), $E_{1/2}$ = 0.70 V (IV/III, $\Delta E$ = 30 mV), and $E_{1/2}$ = 0.88 V (V/IV $\Delta E$ = 39 mV), as shown in Figures S18, S19, and S21.

The redox potential of these couples was analyzed as a function of pH, and a Pourbaix diagram was built, which is presented in Figure 7b. The diagram shows three consecutive PCET events in the range of pH 2−12, with slopes close to the expected ones for one electron and multiple proton transfer processes associated with multiple Ru-aquo groups. Surprisingly, the Pourbaix obtained is very similar to that of *cis*-[Ru(bpy)$_2$(H$_2$O)$_2$]$^{2+}$,[36] with the same number of species but with some slight differences in the redox potentials (see Figure S20B in the SI). Thus, we associate this transformation to the progressive formation of {*cis*-[Ru$^{II}$(H$_2$O)$_2$(bda-$\kappa$-NO)(4,4′-bpy)]$_{10}$(4,4′-bpy)}, **10′(H$_2$O)$_2$**, at the surface of the electrode where the initial tetradentate bda ligands change their coordination mode from $\kappa$-N$^2$O$^2$ to $\kappa$-NO with concomitant coordination of aquo ligands to the positions partially liberated by the bda ligands (Figure 6, bottom). It is also interesting to mention that this transformation only occurs during the electrocatalytic process at the graphitic surface and it does not take place at lower oxidation states (III/II or IV/III; see Figure S23 in the SI) nor in the homogeneous phase for monomeric homologue [Ru(bda)(pic)$_2$],[22] thus manifesting the key role of the graphitic surface to drive this transformation.

We used an EPR spectroelectrochemical cell[37] to follow the paramagnetic signature of **10** and **10′(H$_2$O)$_2$** as well as their derived species immobilized on the electrode surface of a carbon paper (**10@C-paper**), at different oxidation states. The main spectra obtained are displayed in Figure 8. Measurement of a freshly formed film (**Ru$^{II}$-10@C-paper**) reveals only an


https://doi.org/10.1021/jacs.1c04738
J. Am. Chem. Soc. 2021, 143, 11651−11661

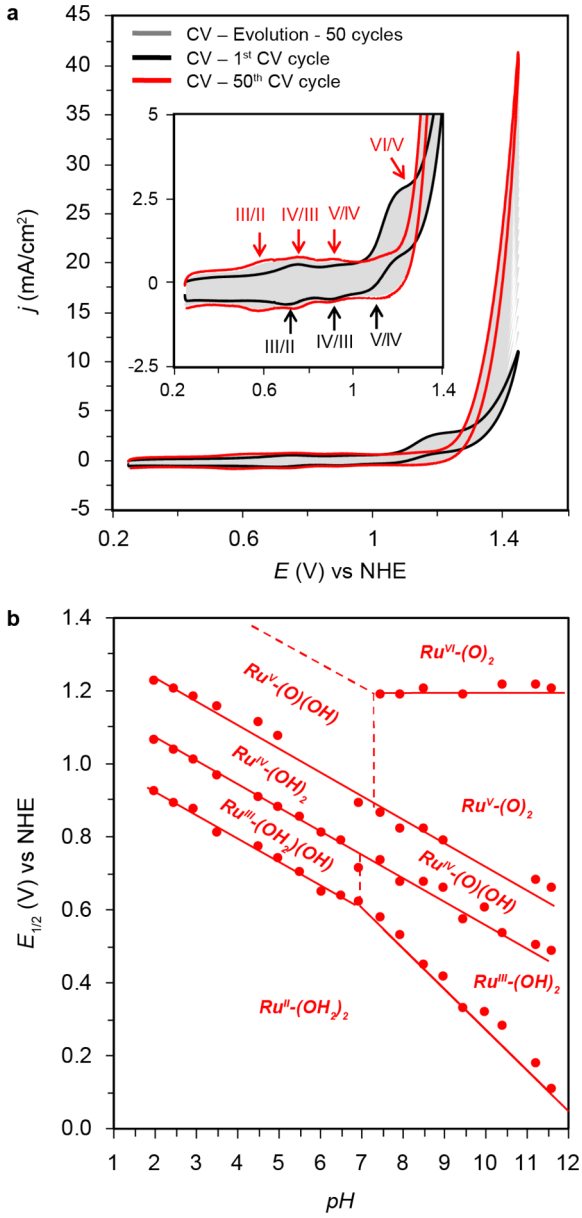


**Figure 7.** (a) CV evolution of **10@CNT@GC** ($\Gamma_{10}$ = 2.3 nmol·cm$^{-2}$) to form **10′(H$_2$O)$_2$@CNT@GC** ($\Gamma_{10'(H2O)2}$ = 1.6 nmol·cm$^{-2}$) during 50 repetitive CV cycles in 1 M phosphate buffer (pH 7) at a scan rate of 100 mV/s. The black line corresponds to the first cycle, the gray line to the second to 49th cycles, and the red line to the 50th cycle. Inset: enlargement of the noncatalytic redox waves. (b) Pourbaix diagram of **10′(H$_2$O)$_2$@CNT@GC**.

EPR spectrum identical to when the bare carbon paper is measured, with a sharp signal assigned to radical species on C-paper (Figure S36).

After applying 0.7 V for 10 min an additional anisotropic signal with $g$ = [2.27, 2.12, 1.85] appears, in agreement with the formation of the $S$ = 1/2 {[Ru$^{III}$(OH)(bda)(4,4′-bpy)]$_{10}$(4,4′-bpy)} species, **Ru$^{III}$-10@C-paper**. We did not identify any spin−spin interaction between neighboring Ru centers, probably due to the long distance (11.3 Å). Increasing the potential to 0.9 V just lowers the intensity of this signal, as EPR-silent Ru$^{IV}$ species are formed. Interestingly, the $g$ values of the signal assigned to the Ru$^{III}$ species shift to $g$ = [2.45, 2.24, 1.85] after the electrode was cycled 50 times. This

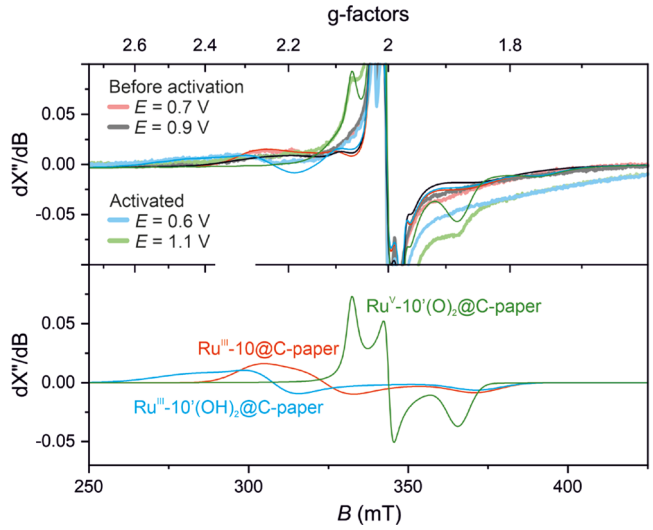


**Figure 8.** EPR spectra (upper panel, thick shaded traces) measured *in situ* before and after electrochemical activation (by running 50 CVs between 0.2 and 1.2 V), on a carbon paper electrode functionalized with **10** (**10@C-paper**); see the SI and Figure S37 for details. The spectra can be simulated with a combination of two main components, a signal centered around $g$ = 2.0, assigned to the carbon paper (Figure S36), and the anisotropic Ru signals (present only after catalyst adsorption). Spectra were measured at 10 K in 0.1 phosphate buffer (pH 7.0).

increase of anisotropy is consistent with the formation of {[Ru$^{III}$(OH)$_2$(bda-κ-NO)(4,4′-bpy)]$_{10}$(4,4′-bpy)} species, **Ru$^{III}$-10′(OH)$_2$@C-paper**. It is interesting to note that for [Ru(bda)(py)$_2$] complexes the species responsible for catalysis needs to reach oxidation state V. However, in *cis*-[Ru(bpy)$_2$(H$_2$O)$_2$]$^{2+}$, the presence of two aqua ligands bonded to the Ru aqua center stabilizes the Ru(V) oxidation state and water oxidation catalysis occurs only at the formal oxidation state VI.[38] This allows the spectroscopic characterization of the Ru(V) species before catalysis occurs.[39] Similarly, the oxidation of **Ru$^{III}$-10′(OH)$_2$@C-paper** at 1.1 V generates the **Ru$^{V}$-10′(O)$_2$@C-paper** species ($g$ = [2.07, 2.00, 1.88]), the EPR spectrum of which is reported in Figure 8. These $g$-factors are in good agreement with previously reported Ru$^{III}$ and Ru$^{V}$ complexes.[39−41]

The proposed transformation was further analyzed by DFT calculations[32b,35] where several options were considered. DFT discarded both a seven-coordinated Ru species and κ-N$^2$-coordinated bda in **10′(H$_2$O)$_2$@CNT**, since the respective minima on the potential energy surface are much higher than for bda-κ-NO coordination (Table S9) at the Ru(V) oxidation state, where the crucial transformation step occurs according to CV. Indeed, the addition of two water molecules to Ru(II) is strongly endergonic, with a calculated free energy difference of 101.7 kJ/mol, while a value of only 9.1 kJ/mol is obtained for Ru(V) (Figure S43). Since the employed monomeric model compounds do not include the effects of changing noncovalent interaction energy between catalyst and graphitic surface during the activation procedure, the latter has to be evaluated separately. For this purpose, we performed quantum chemical calculations on a semiempirical level employing a dimeric model of **10′(H$_2$O)$_2$**, {[Ru$^{II}$(H$_2$O)$_2$(bda-κ-NO)(py)]$_2$(μ-4,4′-bpy)}, **2(H$_2$O)$_2$**, anchored on a sufficiently large hexagonal graphene sheet, **2(H$_2$O)$_2$@GS**. As illustrated in Figure 6, now besides the CH−π interactions observed for **2@GS**, the


https://doi.org/10.1021/jacs.1c04738
J. Am. Chem. Soc. 2021, 143, 11651−11661

formation of $\mathbf{2(H_2O)_2@GS}$ introduces additional $\pi-\pi$ interactions between the graphitic surface and the bda axial pyridyl moiety, which is further favored by the hydrogen bonding between the Ru-OH group and the dangling carboxylate (see Figure 6). Additionally, free carboxylates are stabilized by anion$-\pi$ interactions, although this effect is assumed to play a minor role in higher oxidation states due to proton sharing with aquo ligands via hydrogen bonds. In total, the interaction is enhanced during this transformation by 12.9 kJ/mol per Ru center. Although this value has been determined for Ru(II), it can be assumed to be approximately constant in all oxidation states and, as a result, compensating the energy needed to incorporate a second water molecule in the Ru(V) state (9.1 kJ/mol) as described above. This explains why this transformation process only occurs under the influence of the graphitic surface. Since a large barrier of 150.2 kJ/mol (Figure S43b) is involved in this transition, this process is slow, which explains the large number of necessary CV cycles in order to achieve complete conversion into $\mathbf{10'(H_2O)_2@CNT}$, but also, once formed, it displays high stability at the electrode surface. Further, the X-ray absorption spectroscopy (XAS) experiments (red and cyan traces in Figure 2; Tables S5−S7) are also consistent with this transformation.

Using the information from the Pourbaix diagram in Figure 7b, DFT has been used to study the complete water oxidation mechanism starting from the monomer *cis*-$[Ru^{II}(H_2O)_2(bda\text{-}\kappa\text{-}NO)(py)_2]$, $\mathbf{1'(H_2O)_2}$, as depicted in Figure 9a. All calculated redox potentials are remarkably low, supporting the assumption that $\mathbf{1'(H_2O)_2}$ is a suitable model for $\mathbf{10'(H_2O)_2@CNT@GC}$ and the respective coordination environment of Ru (Table S8). Especially, the obtained values for $Ru^{IV}/Ru^{III}$, $Ru^{V}/Ru^{IV}$, and $Ru^{VI}/Ru^{V}$ redox pairs are properly fitting to the experimental data at neutral pH.

Notably, a strong hydrogen bond between one of the aquo ligands and the dangling carboxy group helps intramolecular charge delocalization. The deviation in the calculated $Ru^{III}/Ru^{II}$ potential can be explained by the neglect of the graphitic surface in the employed model system. Missing anion$-\pi$ interaction leads to protonation of the carboxy group already in Ru(II) and overestimation of the free energy of the latter species, therefore suggesting a $1e^-/1H^+$ proton-coupled electron transfer (PCET) for the $Ru^{III}/Ru^{II}$ pair in $\mathbf{1'(H_2O)_2}$, contrary to the experimental findings for $\mathbf{10'(H_2O)_2@CNT}$. The intramolecular proton transfer is especially important in higher oxidation states, since it allows access to an exceptionally stable $Ru^{V}(O)_2$ species. Formation of this complex is accompanied by further decoordination of the equatorial ligand to form a trigonal bipyramidal bda-$\kappa$-O complex, reducing the formal number of electrons in the coordination environment from 19 to 17. WNA would be energetically strongly uphill in this state ($\Delta G$ = 129.7 kJ/mol, Figure S45a); thus a fourth oxidation up to formal $Ru^{VI}$ is necessary (as observed experimentally here and for $[Ru(bpy)_2(H_2O)_2]^{2+}$ as well)[38] to allow formation of the O−O bond. In this step, two different oxo groups, $O^1$ or $O^2$, could be attacked by water according to the numbering in Figure 9b. Although it cannot be excluded that in this step WNA happens on oxo group $O^2$ to some extent in the equilibrium, this is less probable because of its more negative partial charge compared to $O^1$ (Figure S45b). A transition state with the dangling carboxylate directly acting as a base for the attacking water, as it has been discussed for $[Ru(tda)(py)_2]$ catalysts,[42] is

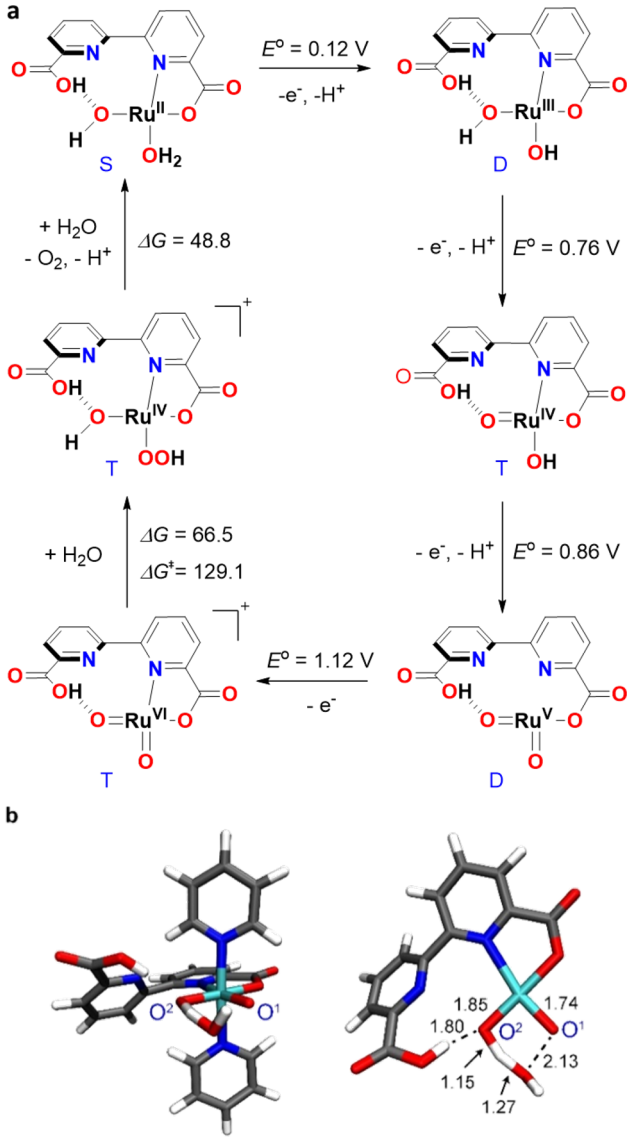


**Figure 9.** (a) Water oxidation mechanism of $\mathbf{1(H_2O)_2}$ proposed based on calculations on the B3LYP-D3/def2-SVP level of theory including implicit water solvation. Redox potentials are provided vs standard hydrogen electrode. Free energies are given in kJ/mol. Blue letters correspond to the lowest spin state. Pyridine axial ligands have been omitted for clarity in all drawn structures. (b) Side view and top view of the optimized transition state of the WNA with omitted axial ligands for clarity. Relevant bond lengths in Å are provided as black numbers. Blue labels correspond to the numbering of oxo groups used in the text. For a detailed description of all calculations and chosen model systems, see the SI.

therefore unlikely to occur and could not be identified by our optimization attempts. Instead, it can be seen from the optimized transition state depicted in Figure 9b that the oxygen atom of the water attacks $O^1$ while $O^2$ serves as an immediate proton acceptor, which is in line with former studies of WNA on $Ru^{VI}(O)_2$.[38]

In acidic media, however, the ability of intramolecular proton transfer to the carboxylate is reduced because of external protonation of the latter. Thus, $O^2$ would be already protonated and as a consequence unable to support the WNA step, which explains the loss in activity of the presented system below pH 5.5 (Figure S22). Further, it is worth noting that the


https://doi.org/10.1021/jacs.1c04738
J. Am. Chem. Soc. 2021, 143, 11651−11661

**Scheme 1. Summary of Proposed Redox Events for 10@CNT@GC and 10′$(H_2O)_2$@CNT@GC at pH 7**[a]

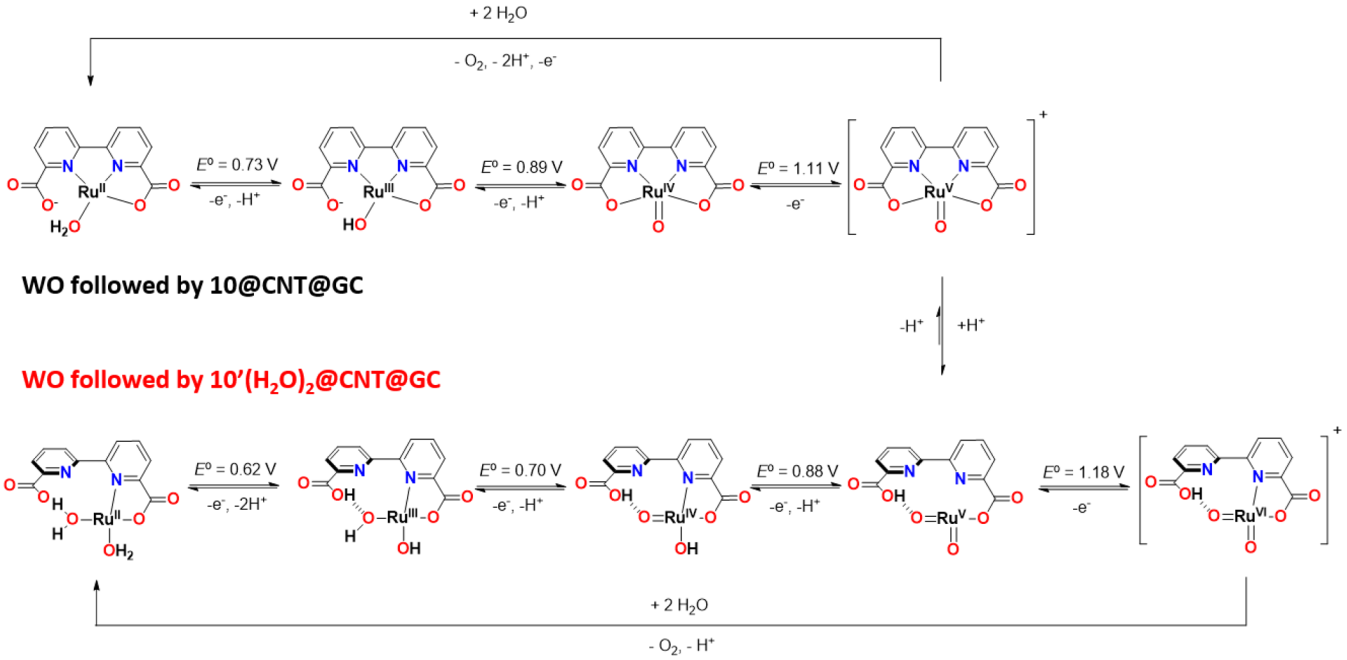


[a]Pyridine axial ligands have been omitted for clarity.

electrochemical oxidation up to $Ru^{VI}(O)_2$ directly leads to a high-spin triplet species. Since this spin state is preserved in the following intermediates, no additional intersystem crossing is necessary to close the catalytic cycle and release triplet dioxygen. This way, a potential additional barrier associated with change of the spin state is avoided.

The proposed scenario for **10** is summarized in Scheme 1, where after three consecutive one-electron transfers **10@CNT** is able to oxidize water to dioxygen during initial CV cycles. However, upon repetitive cycling, the intensity of the catalytic wave located at $E_{onset} \approx 1.02$ V decreases drastically, accompanied by a shift of the foot of the electrocatalytic wave to $E_{onset} \approx 1.10$ V. This fact is provoked by a rearrangement of coordination environment for Ru-bda on graphitic surfaces, which favor the high-stabilized open-ring species due to the strong CH−$\pi$ and $\pi$−$\pi$ interactions with CNTs. Successively, the new "bda-$\kappa$-NO" coordination environment promotes the introduction of a second aquo ligand in the first coordination sphere, forming **10′$(H_2O)_2$@CNT**. Thus, a new catalytic cycle comes into play, where Ru(VI) is the species responsible for O−O bond formation, thanks to the high stabilization effect of three consecutive PCET events, the intramolecular hydrogen bonding, and the additional stabilization energy provided by the graphitic surface.

**Performance of 10′$(H_2O)_2$@CNT as a Molecular Water Oxidation Anode.** In the previous section, we have shown that upon repetitive CVs the molecular water oxidation catalyst **10** anchored on the CNT is progressively transformed into a more powerful catalyst, **10′$(H_2O)_2$**, which reaches current densities of 42 mA/cm$^2$ at 1.45 V, as shown in Figure 7a. Increasing the amount of mass deposited on the electrode surface, we obtained **10′$(H_2O)_2$@CNT@GC** molecular anodes with a surface density of $\Gamma_{10'(H2O)2}$ = 12.2 nmol·cm$^{-2}$, which reach remarkable current densities in the range of 180 mA/cm$^2$ at 1.45 V, as shown in Figure 10a (see Figures S25−S27 and Table S3). To kinetically characterize the electrocatalytic performance of these materials, we carried out a foot of the wave analysis (FOWA), which is shown in Figure 10a and Figures S29 and S30.[43] A $TOF_{max}$ average value of 3.7 × $10^3$ ± 0.36 × $10^3$ $s^{-1}$ is obtained for several samples of different degrees of surface loading with a kinetic rate law that is first order with regard to the [Ru] at the surface ($\Gamma_{Ru}$). A CPE experiment was carried out using **10′$(H_2O)_2$@CNT@GC** ($\Gamma_{10'(H2O)2}$ = 16.7 nmol·cm$^{-2}$) at an applied potential of $E_{app}$ = 1.35 V (Figure 10b).

A very stable current density of 14 mA/cm$^2$ was generated for 12 h, which implies a turnover number TON = 9.4 × $10^4$ per Ru unit assuming 94% faradaic efficiency. The latter was calculated using a Clark-type electrode in the gas phase, as shown in Figure S31. The integrity of the catalyst after 9.4 × $10^4$ TONs was evaluated based on CV experiments that showed no additional species generated during turnover and thus manifests its high stability (Figure S28). In addition, XAS experiments displayed in Figure 2 further support that the molecular species before and after catalysis are the same (cyan and magenta traces in Figure 2) and, importantly, also ruling out the formation of $RuO_2$ (see also Figures S32 and S33). This is remarkable considering that in the homogeneous phase the *cis*-$[Ru(bpy)_2(H_2O)_2]^{2+}$ complex has a high tendency to isomerize to its *trans* form, which does not have the sufficiently high redox potentials to undergo water oxidation catalysis. This isomerization phenomenon is therefore responsible for the low activity of *cis*-$[Ru(bpy)_2(H_2O)_2]^{2+}$ as a water oxidation catalyst.[38,39] In sharp contrast, here the *cis*-bis-aquo complex **10′$(H_2O)_2$@CNT@GC** is perfectly stable under turnover and does not isomerize, thanks again to the stabilizing effect of the surface interactions.

The performance of **10′$(H_2O)_2$@CNT@GC** as a molecular anode for water oxidation is comparable to that of the recently reported activated $(Ru\text{-}tda)_{15}$@CNT@GC in terms of TONs and a bit lower regarding TOFs.[30] The latter also relies on


https://doi.org/10.1021/jacs.1c04738
J. Am. Chem. Soc. 2021, 143, 11651−11661

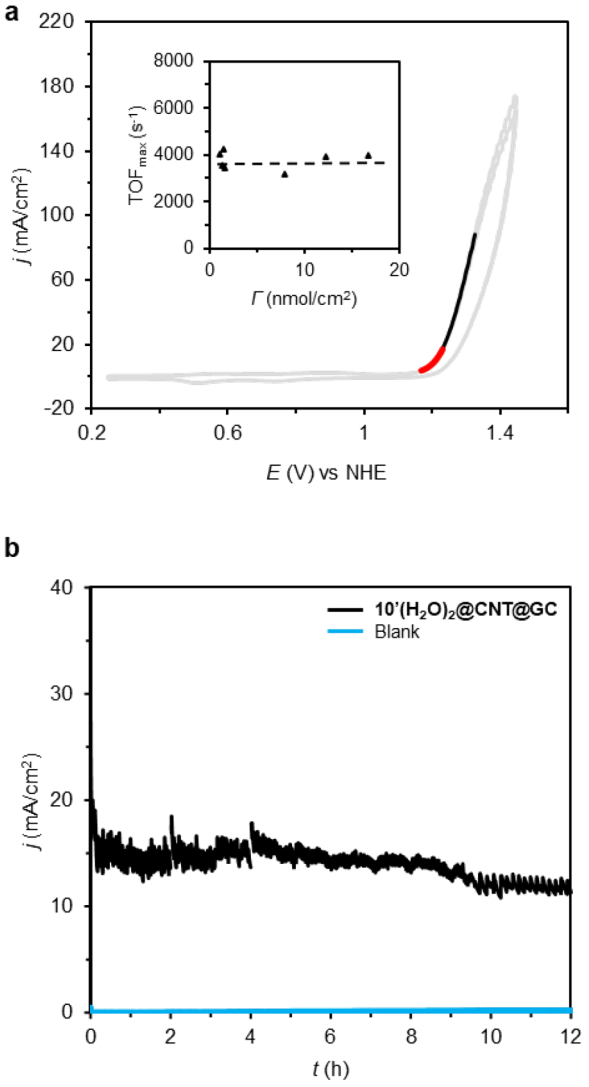


**Figure 10.** (a) CV of **10′(H$_2$O)$_2$@CNT@GC** in 1.0 M phosphate buffer (pH 7) at a scan rate of 100 mV/s (gray trace). The black line corresponds to the experimental data used for FOWA analysis, and the red line shows the region used for the determination of the TOF$_{max}$ value. Inset: Plot of TOF$_{max}$ vs $\Gamma_{10'(H2O)2}$. (b) CPE of **10′(H$_2$O)$_2$@CNT@GC** ($\Gamma_{10'(H2O)2}$ = 16.7 nmol·cm$^{-2}$) at $E_{app}$ = 1.35 V vs NHE in a 1 M phbf (pH 7) solution for 12 h (black trace) and blank (blue trace).

aromatic CH−$\pi$ interactions with a CNT surface for anchoring purposes. Additionally, the present system benefits from the fact that it does not need an activation process in basic solution, as is the case for (Ru-tda)$_{15}$@CNT@GC. It is worth mentioning that the CH−$\pi$ interaction used here achieves surface densities that are at least 2 orders of magnitude higher than traditional anchoring strategies based on $\pi$−$\pi$ stacking or on the use of diazonium salts, as observed for other molecular water oxidation catalysts (see Table S4).[44−46] This in turn allows reaching current densities that are more than 2 orders of magnitude higher than the ones obtained using these traditional methods, and it provides a remarkable stability.[26]

This is in sharp contrast with the paradigm established when using oxides as water oxidation catalysts, where an increase in the amount of mass generates an interfacial instability that limits the anode performance.[47] Additionally, current densities in the range of 0.2 A/cm$^2$ using metal oxides as catalysts are only obtained at pH 13 or above with a very large amount of metal oxide deposited at the surface of the electrode.[48] Further, coordination polymers based on bridging ligands and using Fe and Ni as transition metals have been reported as efficient water oxidation anodes using approximately $\Gamma$ = 17 $\mu$mols/cm$^2$ of Fe$_2$Ni on top of a Ni foam electrode.[49] At pH 14, these electrodes achieve current densities of 100 $\mu$A/cm$^2$ with approximately 300 mV overpotential. In sharp contrast, here in our work we deposit 0.1 nmol/cm$^2$ of Ru at the GC electrode and 16.7 nmols/cm$^2$ at the CNTs, which is 5 and 3 orders of magnitude less mass as compared to the previously mentioned Ni foam electrode.

## CONCLUSIONS

A Ru-bda oligomer with 10 repetitive units of formula {[Ru$^{II}$(bda-$\kappa$-N$^2$O$^2$)(4,4′-bpy)]$_{10}$(4,4′-bpy)}, **10**, has been prepared, thoroughly characterized, and successfully anchored onto CNTs taking advantage of CH−$\pi$ interactions between the bda ligand and graphitic surfaces. Anchored on CNTs, **10** behaves as a molecular electrocatalytic anode but progressively evolves to a new complex where the bda ligands change their coordination mode from bda-$\kappa$-N$^2$O$^2$ to bda-$\kappa$-NO, generating the new molecular hybrid material, **10′(H$_2$O)$_2$@CNT**. This transformation is facilitated by the interaction of the bda ligand with graphitic surfaces favoring a partial decoordination via additional $\pi$−$\pi$ and anion−$\pi$ interactions. This ligand flexibility is in turn responsible for the high stability of the oligomer on the surface of CNTs.

The new molecular hybrid material **10′(H$_2$O)$_2$@CNT** achieves current densities in the range of 200 mA/cm$^2$ at pH 7 under an applied potential of 1.45 V, using very small amounts of mass (0.1 nmol/cm$^2$ of Ru at the GC electrode and 16.7 nmol/cm$^2$ at the CNTs) with TOFs and TONs in the range of 3.7 × 10$^4$ s$^{-1}$ and 9.4 × 10$^4$, respectively. The high activity of the complex is associated with the ligand flexibility and the second coordination sphere effects exerted by the decoordinated arm of the bda ligand that provides the necessary stabilization by H-bonding for a low-energy catalytic cycle. On the other hand, the high stability of the Ru water oxidation catalyst is associated with the molecular catalyst−surface interactions especially during turnover. The oligomeric nature of the molecule provides multiple sites of anchorage at the surface, which strongly enhances the overall stability of the hybrid catalyst−CNT anode via a dynamic bonding.

## ASSOCIATED CONTENT

### Supporting Information

The Supporting Information is available free of charge at https://pubs.acs.org/doi/10.1021/jacs.1c04738.

Experimental procedures, additional spectroscopic, microscopy, and electrochemical data, and computational details (PDF)

## AUTHOR INFORMATION

### Corresponding Authors

**Antoni Llobet** − *Institute of Chemical Research of Catalonia (ICIQ). Barcelona Institute of Science and Technology (BIST), 43007 Tarragona, Spain; Departament de Quimica, Universitat Autonoma de Barcelona, 08193 Barcelona, Spain;* orcid.org/0000-0002-6176-5272; Email: allobet@iciq.cat



https://doi.org/10.1021/jacs.1c04738
J. Am. Chem. Soc. 2021, 143, 11651−11661

**Frank Würthner** − *Center for Nanosystems Chemistry, 97074 Würzburg, Germany; Institut für Organische Chemie, Universität Würzburg, 97074 Würzburg, Germany;* orcid.org/0000-0001-7245-0471; Email: wuerthner@uni-wuerzburg.de

### Authors

**Marcos Gil-Sepulcre** − *Institute of Chemical Research of Catalonia (ICIQ). Barcelona Institute of Science and Technology (BIST), 43007 Tarragona, Spain;* orcid.org/0000-0002-2839-8108

**Joachim O. Lindner** − *Center for Nanosystems Chemistry, 97074 Würzburg, Germany*

**Dorothee Schindler** − *Institut für Organische Chemie, Universität Würzburg, 97074 Würzburg, Germany*

**Lucía Velasco** − *Instituto Madrileño de Estudios Avanzados en Nanociencia (IMDEA-Nanociencia), 28049 Madrid, Spain*

**Dooshaye Moonshiram** − *Instituto Madrileño de Estudios Avanzados en Nanociencia (IMDEA-Nanociencia), 28049 Madrid, Spain;* orcid.org/0000-0002-9075-3035

**Olaf Rüdiger** − *Max Planck Institute for Chemical Energy Conversion, 45470 Mülheim an der Ruhr, Germany;* orcid.org/0000-0002-5148-9083

**Serena DeBeer** − *Max Planck Institute for Chemical Energy Conversion, 45470 Mülheim an der Ruhr, Germany;* orcid.org/0000-0002-5196-3400

**Vladimir Stepanenko** − *Center for Nanosystems Chemistry, 97074 Würzburg, Germany; Institut für Organische Chemie, Universität Würzburg, 97074 Würzburg, Germany*

**Eduardo Solano** − *NCD-SWEET beamline, ALBA synchrotron light source, 08290 Barcelona, Spain;* orcid.org/0000-0002-2348-2271

Complete contact information is available at: https://pubs.acs.org/10.1021/jacs.1c04738

### Author Contributions

M.G.-S. performed the synthesis, characterization, and electrochemical experiments and coordinated the tasks with all authors. J.O.L. performed the computational studies. D.S. assisted in the analysis of the results. L.V. and D.M. performed the XANES and EXAFS measurements and data analysis. O.R. performed EPR measurements and data analysis. V.S. performed the AFM and SEM experiments. E.S. assisted in the analysis of X-ray scattering results. F.W. and A.L. conceived the idea of the project and wrote the paper. All authors contributed to the design of experiments, analysis of the results, and preparation of the manuscript.

### Notes

The authors declare no competing financial interest.

## ■ ACKNOWLEDGMENTS

This project has received funding from the European Research Council (ERC) under the European Union's Horizon 2020 research and innovation program (grant agreement No. 787937, recipient F.W.). We thank the Alexander von Humboldt Foundation for supporting this collaborative research with a Humboldt research award for A.L. A.L. also acknowledges support from Ministerio de Ciencia e Innovación, Severo Ochoa Excellence Acreditation, FEDER, and AGAUR through grants PID2019-111617RB-I00, CEX2019-000925-S, and 2017-SGR-163. D.M. acknowledges funding from the Severo Ochoa Excellence Program from the Instituto IMDEA Nanociencia, the Acciones de Dinamización "Europa Investigacion" grant (EIN2019-103399), and the Spanish Ministerio de Ciencia, Innovacion y Universidades grant (PID2019-111086RA-I00). O.R. and S.D. thank the Max Planck Society for funding and Eckhard Bill for support with the EPR simulations. This research used resources of the Advanced Photon Source (Beamline 9 $\mu_B$-B), an Office of Science User Facility operated for the U.S. Department of Energy (DOE) Office of Science by Argonne National Laboratory, and was supported by the U.S. DOE under Contract No. DE-AC02-06CH11357. Synchrotron X-ray scattering experiments were performed at NCD-SWEET beamline at ALBA synchrotron with the collaboration of ALBA staff (Proposal 2020094629).

## ■ REFERENCES

(1) Steffen, W.; Rockström, J.; Richardson, K.; Lenton, T. M.; Folke, C.; Liverman, C.; Summerhayes, C. P.; Barnosky, A. D.; Cornell, S. E.; Crucifix, M.; Donges, J. F.; Fetzer, I.; Lade, S. J.; Scheffer, M.; Winkelmann, R.; Schellnhuber, H. J. Trajectories of the Earth System in the Anthropocene. *Proc. Natl. Acad. Sci. U. S. A.* **2018**, *115*, 8252−8259.

(2) Balmaseda, M. A.; Trenberth, K. E.; Källén, E. Distinctive climate signals in reanalysis of global ocean heat content. *Geophys. Res. Lett.* **2013**, *40*, 1754−1759.

(3) Edenhofer, O.; Pichs-Madruga, R.; Sokona, Y.; Minx, J. C.; Farahani, E.; Kadner, S.; Seyboth, K.; Adler, A.; Baum, I.; Brunner, S.; Eickemeier, P.; Kriemann, B.; Savolainen, J.; Schlömer, S.; Stechow, C. V.; Zwickel, T. The Intergovernmental Panel on Climate Change (IPCC). *Climate Change 2014: Mitigation of Climate*; Cambridge Univ. Press, 2014.

(4) Frischmann, P. D.; Mahata, K.; Würthner, F. Powering the future of molecular artificial photosynthesis with light-harvesting metallosupramolecular dye assemblies. *Chem. Soc. Rev.* **2013**, *42*, 1847−1870.

(5) Sala, X.; Maji, S.; Bofill, R.; García-Antón, J.; Escriche, L.; Llobet, A. Molecular Water Oxidation Mechanisms Followed by Transition Metals: State of the Art. *Acc. Chem. Res.* **2014**, *47*, 504−516.

(6) Smith, R. D. L.; Prévot, M. S.; Fagan, R. D.; Zhang, Z.; Sedach, P. A.; Siu, M. K. J.; Trudel, S.; Berlinguette, C. P. Photochemical Route for Accessing Amorphous Metal Oxide Materials for Water Oxidation Catalysis. *Science* **2013**, *340*, 60−63.

(7) McCrory, C. C. L.; Jung, S.; Peters, J. C.; Jaramillo, T. F. Benchmarking Heterogeneous Electrocatalysts for the Oxygen Evolution Reaction. *J. Am. Chem. Soc.* **2013**, *135*, 16977−16987.

(8) McCrory, C. C. L.; Jung, S.; Ferrer, I. M.; Chatman, S. M.; Peters, J. C.; Jaramillo, T. F. Benchmarking Hydrogen Evolving Reaction and Oxygen Evolving Reaction Electrocatalysts for Solar Water Splitting Devices. *J. Am. Chem. Soc.* **2015**, *137*, 4347−4357.

(9) Mohammed-Ibrahim, J. A. review on NiFe-based electrocatalysts for efficient alkaline oxygen evolution reaction. *J. Power Sources* **2020**, *448*, 227375.

(10) Walter, M. G.; Warren, E. L.; McKone, J. R.; Boettcher, S. W.; Mi, Q.; Santori, E. A.; Lewis, N. Solar Water Splitting Cells. *Chem. Rev.* **2010**, *110*, 6446−6473.

(11) Kärkäs, M. D.; Verho, O.; Johnston, E. V.; Åkermark, B. Artificial Photosynthesis: Molecular Systems for Catalytic Water Oxidation. *Chem. Rev.* **2014**, *114*, 11863−12001.

(12) Berardi, S.; Drouet, S.; Francàs, L.; Gimbert-Suriñach, C.; Guttentag, M.; Richmond, C.; Stoll, T.; Llobet, A. Molecular artificial photosynthesis. *Chem. Soc. Rev.* **2014**, *43*, 7501−7519.

(13) Blakemore, J. D.; Crabtree, R. H.; Brudvig, G. W. Molecular Catalysts for Water Oxidation. *Chem. Rev.* **2015**, *115*, 12974−13005.

(14) Garrido-Barros, P.; Gimbert-Suriñach, C.; Matheu, R.; Sala, X.; Llobet, A. How to make an efficient and robust molecular catalyst for water oxidation. *Chem. Soc. Rev.* **2017**, *46*, 6088−6098.

(15) Matheu, R.; Garrido-Barros, P.; Gil-Sepulcre, M.; Ertem, M. Z.; Sala, X.; Gimbert-Suriñach, C.; Llobet, A. The development of molecular water oxidation catalysts. *Nat. Rev. Chem.* **2019**, *3*, 331−341.
(16) Li, X.; Lei, H.; Liu, J.; Zhao, X.; Ding, S.; Zhang, Z.; Tao, X.; Zhang, W.; Wang, W.; Zheng, X.; Cao, R. Carbon Nanotubes with Cobalt Corroles for Hydrogen and Oxygen Evolution in pH 0−14 Solutions. *Angew. Chem., Int. Ed.* **2018**, *57*, 15070−15075.
(17) Xie, L.; Li, X.; Wang, B.; Meng, J.; Lei, H.; Zhang, W.; Cao, R. Molecular Engineering of a 3D Self-Supported Electrode for Oxygen Electrocatalysis in Neutral Media. *Angew. Chem., Int. Ed.* **2019**, *58*, 18883−18887.
(18) Xu, J.; Murphy, S.; Xiong, D.; Cai, R.; Wei, X.-K.; Heggen, M.; Barborini, E.; Vinati, S.; Dunin-Borkowski, R. E.; Palmer, R. E.; Liu, L. Cluster Beam Deposition of Ultrafine Cobalt and Ruthenium Clusters for Efficient and Stable Oxygen Evolution Reaction. *ACS Appl. Energy Mater.* **2018**, *1*, 3013−3018.
(19) Li, W.; Gao, X.; Wang, X.; Xiong, D.; Huang, P.-P.; Song, W.-G.; Bao, X.; Liu, L. From water reduction to oxidation: Janus Co-Ni-P nanowires as high efficiency and ultrastable electrocatalysts for over 3000 h water splitting. *J. Power Sources* **2016**, *330*, 156−166.
(20) Garrido-Barros, P.; Gimbert-Suriñach, C.; Moonshiram, D.; Picón, A.; Monge, P.; Batista, V. S.; Llobet, A. Electronic π-Delocalization Boosts Catalytic Water Oxidation by Cu(II) Molecular Catalysts Heterogenized on Graphene Sheets. *J. Am. Chem. Soc.* **2017**, *139*, 12907−12910.
(21) Duan, L.; Fischer, A.; Xu, Y.; Sun, L. Isolated Seven-Coordinate Ru(IV) Dimer Complex with $[HOHOH]^-$ Bridging Ligand as an Intermediate for Catalytic Water Oxidation. *J. Am. Chem. Soc.* **2009**, *131*, 10397−10399.
(22) Duan, L.; Bozoglian, F.; Mandal, S.; Steward, B.; Privalov, T.; Llobet, A.; Sun, L. A molecular ruthenium catalyst with water-oxidation activity comparable to that of photosystem II. *Nat. Chem.* **2012**, *4*, 418−423.
(23) Zhang, B.; Sun, L. Ru-bda: Unique Molecular Water-Oxidation Catalysts with Distortion Induced Open Site and Negatively Charged Ligands. *J. Am. Chem. Soc.* **2019**, *141*, 5565−5580.
(24) Matheu, R.; Ertem, M. Z.; Gimbert-Suriñach, C.; Sala, X.; Llobet, A. Seven Coordinated Molecular Ruthenium−Water Oxidation Catalysts: A Coordination Chemistry Journey. *Chem. Rev.* **2019**, *119*, 3453−3471.
(25) Matheu, R.; Ertem, M. Z.; Gimbert-Suriñach, C.; Benet-Buchholz, J.; Sala, X.; Llobet, A. Hydrogen Bonding Rescues Overpotential in Seven-Coordinated Ru Water Oxidation Catalysts. *ACS Catal.* **2017**, *7*, 6525−6532.
(26) Li, F.; Zhang, B.; Li, X.; Jiang, Y.; Chen, L.; Li, Y.; Sun, L. Highly Efficient Oxidation of Water by a Molecular Catalyst Immobilized on Carbon Nanotubes. *Angew. Chem., Int. Ed.* **2011**, *50*, 12276−12279.
(27) Wang, L.; Fan, K.; Chen, H.; Daniel, Q.; Philippe, B.; Rensmo, H.; Sun, L. Towards efficient and robust anodes for water splitting: Immobilization of Ru catalysts on carbon electrode and hematite by in situ polymerization. *Catal. Today* **2017**, *290*, 73−77.
(28) Creus, J.; Matheu, R.; Peñafiel, I.; Moonshiram, D.; Blondeau, P.; Benet-Buchholz, J.; García-Antón, J.; Sala, X.; Godard, C.; Llobet, A. A Million TurnoverMolecular Anode for CatalyticWater Oxidation. *Angew. Chem., Int. Ed.* **2016**, *55*, 15382−15386.
(29) Matheu, R.; Francàs, L.; Chernev, P.; Ertem, M. Z.; Batista, V.; Haumann, M.; Sala, X.; Llobet, A. Behavior of the Ru-bda Water Oxidation Catalyst Covalently Anchored on Glassy Carbon Electrodes. *ACS Catal.* **2015**, *5*, 3422−3429.
(30) Hoque, Md. A.; Gil-Sepulcre, M.; de Aguirre, A.; Elemans, J. A. A. W.; Moonshiram, D.; Matheu, R.; Shi, Y.; Benet-Buchholz, J.; Sala, X.; Malfois, M.; Solano, E.; Lim, J.; Garzón-Manjón, A.; Scheu, C.; Lanza, M.; Maseras, F.; Gimbert-Suriñach, C.; Llobet, A. Water oxidation electrocatalysis using ruthenium coordination oligomers adsorbed on multiwalled carbon nanotubes. *Nat. Chem.* **2020**, *12*, 1060−1066.
(31) Schindler, D.; Gil-Sepulcre, M.; Lindner, J. O.; Stepanenko, V.; Moonshiram, D.; Llobet, A.; Würthner, F. Efficient Electrochemical Water Oxidation by a Trinuclear Ru(bda) Macrocycle Immobilized on Multi-Walled Carbon Nanotube Electrodes. *Adv. Energy Mater.* **2020**, *10*, 2002329.
(32) (a) Schulze, M.; Kunz, V.; Frischmann, P. D.; Würthner, F. A. supramolecular ruthenium macrocycle with high catalytic activity for water oxidation that mechanistically mimics photosystem II. *Nat. Chem.* **2016**, *8*, 576−583. (b) Kunz, V.; Lindner, J. O.; Schulze, M.; Röhr, M. I. S.; Schmidt, D.; Mitrić, R.; Würthner, F. Cooperative water oxidation catalysis in a series of trinuclear metallosupramolecular ruthenium macrocycles. *Energy Environ. Sci.* **2017**, *10*, 2137−2153.
(33) Becke, A. D. A new mixing of Hartree−Fock and local density-functional theories. *J. Chem. Phys.* **1993**, *98*, 1372−1377.
(34) Lee, C.; Yang, W.; Parr, R. G. Development of the Colle-Salvetti correlation-energy formula into a functional of the electron density. *Phys. Rev. B: Condens. Matter Mater. Phys.* **1988**, *37*, 785−789.
(35) Schilling, M.; Cunha, R. A.; Luber, S. Enhanced Ab Initio Molecular Dynamics Exploration Unveils the Complex Role of Different Intramolecular Bases on the Water Nucleophilic Attack Mechanism. *ACS Catal.* **2020**, *10*, 7657−7667.
(36) Dobson, J. C.; Meyer, T. J. Redox Properties and Ligand Loss Chemistry in Aqua/Hydroxo/Oxo Complexes Derived from *cis*- and *trans*-$[(bpy)_2Ru^{II}(OH_2)_2]^{2+}$. *Inorg. Chem.* **1988**, *27*, 3283−3291.
(37) Kutin, Y.; Cox, N.; Lubitz, W.; Schnegg, A.; Rüdinger, O. In Situ EPR Characterization of a Cobalt Oxide Water Oxidation Catalyst at Neutral pH. *Catalysts* **2019**, *9*, 926.
(38) Sala, X.; Ertem, M. Z.; Vigara, L.; Todorova, T.; Chen, W.; Rocha, R. C.; Aquilante, F.; Cramer, C. J.; Gagliardi, L.; Llobet, A. The cis-$[Ru^{II}(bpy)_2(H_2O)_2]^{2+}$ Water-Oxidation Catalyst Revisited. *Angew. Chem., Int. Ed.* **2010**, *49*, 7745−7747.
(39) Planas, N.; Vigara, L.; Cady, C.; Miró, P.; Huang, P.; Hammarström, L.; Styring, S.; Leidel, N.; Dau, H.; Haumann, M.; Gagliardi, L.; Cramer, C. J.; Llobet, A. Electronic Structure of Oxidized Complexes Derived from *cis*-$[Ru^{II}(bpy)_2(H_2O)_2]^{2+}$ and Its Photoisomerization Mechanism. *Inorg. Chem.* **2011**, *50*, 11134−11142.
(40) Ezhov, R.; Ravari, A. K.; Page, A.; Pushkar, Y. Water Oxidation Catalyst *cis*-$[Ru(bpy)(5,5'\text{-dcbpy})(H_2O)_2]^{2+}$ and Its Stabilization in Metal−Organic Framework. *ACS Catal.* **2020**, *10*, 5299−5308.
(41) Lebedev, D.; Pineda-Galvan, Y.; Tokimaru, Y.; Fedorov, A.; Kaeffer, N.; Copéret, C.; Pushkar, Y. The Key $Ru^{V}$=O Intermediate of Site-Isolated Mononuclear Water Oxidation Catalyst Detected by in Situ X-ray Absorption Spectroscopy. *J. Am. Chem. Soc.* **2018**, *140*, 451−458.
(42) Matheu, R.; Ertem, M. Z.; Benet-Buchholz, J.; Coronado, E.; Batista, V. S.; Sala, X.; Llobet, A. Intramolecular Proton Transfer Boosts Water Oxidation Catalyzed by a Ru Complex. *J. Am. Chem. Soc.* **2015**, *137*, 10786−10795.
(43) Matheu, R.; Neudeck, S.; Meyer, F.; Sala, X.; Llobet, A. Foot of the Wave Analysis for Mechanistic Elucidation and Benchmarking Applications in Molecular Water Oxidation Catalysis. *ChemSusChem* **2016**, *9*, 3361−3369.
(44) Wu, L.; Nayak, A.; Shao, J.; Meyer, T. J. Crossing the bridge from molecular catalysis to a heterogenous electrode in electrocatalytic water oxidation. *Proc. Natl. Acad. Sci. U. S. A.* **2019**, *116*, 11153−11158.
(45) Wang, L.; Fan, K.; Daniel, Q.; Duan, L.; Li, F.; Philippe, B.; Rensmo, H.; Chen, H.; Sun, J.; Sun, L. Electrochemical driven water oxidation by molecular catalysts *in situ* polymerized on the surface of graphite carbon electrode. *Chem. Commun.* **2015**, *51*, 7883−7886.
(46) Li, F.; Fan, K.; Wang, L.; Daniel, Q.; Duan, L.; Sun, L. Immobilizing Ru(bda) Catalyst on a Photoanode via Electrochemical Polymerization for Light-Driven Water Splitting. *ACS Catal.* **2015**, *5*, 3786−3790.
(47) Weber, D.; Tripkovic, D.; Kretschmer, K.; Bianchini, M.; Brezesinski, T. Surface modification strategies for improving the


https://doi.org/10.1021/jacs.1c04738
J. Am. Chem. Soc. 2021, 143, 11651−11661

cycling performance of Ni-rich cathode materials. *Eur. J. Inorg. Chem.* **2020**, *2020*, 3117−3130.
(48) Xu, J.; Murphy, S.; Xiong, D.; Cai, R.; Wei, X.-K.; Heggen, M.; Barborini, E.; Vinati, S.; Dunin-Borkowski, R. E.; Palmer, R. E.; Liu, L. Cluster Beam Deposition of Ultrafine Cobalt and Ruthenium Clusters for Efficient and Stable Oxygen Evolution Reaction. *ACS Appl. Energy Mater.* **2018**, *1*, 3013−3018.
(49) Ma, J.; Bai, X.; He, W.; Wang, S.; Li, L.; Chen, H.; Wang, T.; Zhang, X.; Li, Y.; Zhang, L.; Chen, J.; Meng, F.; Fu, Y. Amorphous FeNi-bimetallic infinite coordination polymers as advanced electrocatalysts for the oxygen evolution reaction. *Chem. Commun.* **2019**, *55*, 12567−12570.


https://doi.org/10.1021/jacs.1c04738
*J. Am. Chem. Soc.* 2021, 143, 11651−11661